

Statistics of turbulence and intermittency enhancement in superfluid ^4He counterflow

S. Bao^{1,2}, W. Guo^{1,2}, V. S. L'vov³, A. Pomyalov³

¹ National High Magnetic Field Laboratory, 1800 East Paul Dirac Drive, Tallahassee, FL 32310, USA,

² Mechanical Engineering Department, Florida State University, Tallahassee, FL32310, USA,

³ Department of Chemical and Biological Physics,
Weizmann Institute of Science, Rehovot 76100, Israel

We report a detailed analysis of the energy spectra, second- and high-order structure functions of velocity differences in superfluid ^4He counterflow turbulence, measured in a wide range of temperatures and heat fluxes. We show that the one-dimensional energy spectrum $E_{xz}(k_y)$ (averaged over the xz -plane, parallel to the channel wall), directly measured as a function of the wall-normal wave-vector k_y , gives more detailed information on the energy distribution over scales than the corresponding second-order structure function $S_2(\delta_y)$. In particular, we discover two intervals of k_y with different apparent exponents: $E_{xz}(k_y) \propto k_y^{-m_C}$ for $k \lesssim k_\times$ and $E_{xz}(k_y) \propto k_y^{-m_F}$ for $k \gtrsim k_\times$. Here k_\times denotes wavenumber that separate scales with relatively strong (for $k \lesssim k_\times$) and relatively weak (for $k \gtrsim k_\times$) coupling between the normal-fluid and superfluid velocity components. We interpret these k -ranges as *cascade-dominated* and *mutual friction-dominated* intervals, respectively. General behavior of the experimental spectra $E_{xz}(k_y)$ agree well with the predicted spectra [Phys. Rev. B **97**, 214513 (2018)]. Analysis of the n -th order structure functions statistics shows that in the energy-containing interval the statistics of counterflow turbulence is close to Gaussian, similar to the classical hydrodynamic turbulence. In the cascade- and mutual friction-dominated intervals we found some modest enhancement of intermittency with respect of its level in classical turbulence. However, at small scales, the intermittency becomes much stronger than in the classical turbulence.

I. INTRODUCTION

Below the Bose-Einstein condensation temperature $T_\lambda \approx 2.17\text{K}$, liquid ^4He becomes a quantum superfluid¹⁻³ with the vorticity constrained to vortex-line singularities of core radius $a_0 \approx 10^{-8}\text{cm}$ and fixed circulation $\kappa = h/M$ ⁴. Here h is Planck's constant and M is the mass of the ^4He atom. The superfluid turbulence is manifested as a complex tangle of these vortex lines with a typical inter-vortex distance $\ell \sim 10^{-4} - 10^{-2}\text{cm}$ ⁵.

Large-scale hydrodynamics of such system is usually described by a two-fluid model, interpreting ^4He as a mixture of two coupled fluid components: an inviscid superfluid and a viscous normal fluid. The temperature dependent densities of the components $\rho_s(T)$ and $\rho_n(T)$ define their contributions to the mixture. The total density of ^4He $\rho = \rho_s(T) + \rho_n(T) = \rho(T)$ weakly depends on the temperature. The tangle of quantum vortexes mediates the interaction between fluid components via mutual friction force^{2,5-8}.

There is a building evidence⁹⁻¹² that the large-scale turbulence in mechanically driven superfluid ^4He is similar to the classical turbulence. In this case both components move with close velocities being coupled by the mutual friction force almost at all scales. On the contrary, the turbulence generated in superfluid ^4He by a heat flux in a channel has no classical analogy. Here two components are moving in the opposite directions relative to the channel walls, with respective mean velocities \mathbf{U}_n and \mathbf{U}_s . In this way the counterflow velocity $\mathbf{U}_{ns} = \mathbf{U}_n - \mathbf{U}_s \neq 0$, proportional to the applied heat flux, is created along the channel, which can trigger the creation of a tangle of vortex lines above a small critical velocity.

Systematic experimental studies of counterflow turbulence, pioneered by classical 1957-papers of Vinen⁷, were long concentrated mostly on global characteristics of the vortex tangle, cf. see Ref.¹² for a review. The statistics of turbulent fluctuations was not accessible. Recently, the turbulent statistics in the ^4He normal component was measured in the form of the cross-stream 2nd-order structure functions^{13,14}

$$S_2(Y) = \langle |\Delta u_x(Y, y, t)|^2 \rangle . \quad (1a)$$

Here $\langle \dots \rangle$ denotes an ensemble average over many trials and $\Delta u_x(Y, y, t)$ is the streamwise velocity difference

$$\Delta u_x(Y, y, t) = u_x(y + Y, t) - u_x(y, t) . \quad (1b)$$

Other studies^{15,16} measured the statistics of the superfluid component.

Recent theoretical analysis¹⁷ found that the energy spectra in counterflow turbulence are not scale-invariant and cannot be rigorously connected with apparent scaling exponents of the second-order velocity structure functions measured in Ref.¹³ at modest values of the Reynolds numbers. In this paper, we suggest a new way to analyze the visualization data¹³ that allows the one-dimensional energy spectra to be determined so that a direct comparison with theoretical predictions can be made¹⁷. In addition, we use higher-order structure functions to assess the level of intermittency in counterflow turbulence.

The paper is organized as follows:

The analytical background of the problem of statistical description of superfluid counterflow turbulence is covered in Section II. It starts with Sec. II A which is devoted to the second-order statistical characteristics of homogeneous turbulence. In Sec. II B, we suggest a new way of

velocity data analysis that allows to directly extract the one-dimensional energy spectra. The recent analytic theory of counterflow turbulence¹⁷, required for our current analysis, is summarized in Sec. II C. The main result of the theory is the energy-balance Eq. (9) that allows to find the normal-fluid and superfluid energy spectra in a wide range of the problem parameters.

Our experimental results on the statistics of the normal-fluid turbulence and their analysis are presented in Section III. In Sec. III A, we briefly describe the experimental techniques. The important cross-over wavenumbers for the current problem are estimated in Sec. III B. Section III C is devoted to the second-order statistics of counterflow turbulence: the velocity structure functions, $S_2(\delta)$ (see Sec. III C 1 and left column of Fig. 1), and the energy spectra, $E(k)$ (see Sec. III C 2 and middle column of Fig. 1). In particular, we demonstrate that the counterflow energy spectra can be divided in two sub-intervals: a cascade dominated interval and a mutual-friction dominated interval, with the apparent scaling exponents $m_c \simeq 2$ and $m_f \simeq 3$ (see Fig. 1, right column). An important question about the relationship between $S_2(\delta)$ and $E(k)$ is discussed in Sec. III C 3 and illustrated in Fig. 2. We show in Sec. III D and Fig. 3 that the theoretically predicted energy spectra are in good agreement with the experimental energy spectra in the cascade-dominated range of wavenumbers.

In Section III E, we concentrate on high-order velocity structure functions:

$$S_4(Y) = \langle |\Delta u_x(Y, y, t)|^4 \rangle, \quad S_6(Y) = \langle |\Delta u_x(Y, y, t)|^6 \rangle. \quad (1c)$$

In Fig. 4 we show that the flatness $F_4(Y)$ and hyperflatness $F_6(Y)$,

$$F_4(Y) = S_4(Y)/S_2^2(Y), \quad F_6(Y) = S_6(Y)/S_2^3(Y), \quad (2)$$

have two ranges of power-law behavior with an apparent scaling of $F_4(Y) \propto Y^{x_4^{(1),(2)}}$ and $F_6(Y) = S_6(Y)/S_2^3(Y) \propto Y^{x_6^{(1),(2)}}$, respectively. For Y larger than some Y_* that corresponds to the cascade- and mutual friction-dominated subintervals of the energy spectra, $x_4^{(1)} \simeq 0.20$ and $x_6^{(1)} \simeq 0.50$, which are moderately larger than the inertial range exponents in classical hydrodynamic turbulence, i.e., $x_4^{\text{HT}} \simeq 0.14$ and $x_6^{\text{HT}} \simeq 0.38$. However, as Y approaches the viscous scales (i.e., $Y \lesssim Y_*$), the small-scale intermittency becomes stronger: $x_4^{(2)} \simeq 0.5$ and $x_6^{(2)} \simeq 1.4$. This behavior is similar to the intermittency enhancement observed in the mechanically driven ⁴He^{18,19}.

Final Sec. IV briefly summarizes our findings.

II. ANALYTICAL BACKGROUND

A. Second-order statistical characteristics of homogeneous superfluid turbulence

The most general statistical description of the homogeneous superfluid ⁴He turbulent velocity field $\mathbf{u}_j(\mathbf{r})$ at the level of the second-order statistics can be done in the terms of the three-dimensional (3D) cross-correlation functions of the normal-fluid and superfluid turbulent velocity fluctuations in the \mathbf{k} -representation:

$$(2\pi)^3 \delta(\mathbf{k} + \mathbf{k}') F_{ij}^{\alpha\beta}(\mathbf{k}) = \langle v_i^\alpha(\mathbf{k}) v_j^\beta(\mathbf{k}') \rangle. \quad (3a)$$

Here $v_j(\mathbf{k})$ is the Fourier transform of $\mathbf{u}_j(\mathbf{r})$:

$$v_i(\mathbf{k}) = \int \mathbf{u}_i(\mathbf{r}) \exp(i\mathbf{k} \cdot \mathbf{r}) d\mathbf{r}, \quad (3b)$$

$F_j(\mathbf{k}) \equiv F_j^{\alpha\beta}(\mathbf{k})$, $\alpha, \beta = \{x, y, z\}$ are vector indexes, subscripts “ i, j ” denote the normal-fluid ($i, j = \text{n}$) or the superfluid ($i, j = \text{s}$) components, and \mathbf{k} is the wave-vector. The inverse Fourier transform is defined as follows:

$$\mathbf{u}_i(\mathbf{r}) = \int v_i(\mathbf{k}) \exp(-i\mathbf{k} \cdot \mathbf{r}) \frac{d\mathbf{k}}{(2\pi)^3}. \quad (3c)$$

The visualization technique, to be discussed in more details in Sec. III A, allows one to measure the streamwise normal-fluid velocity across a channel, $v_n^x(y, t)$. Henceforth, unless stated explicitly, we consider only this velocity component, i.e. $i, j = \text{n}$, $\alpha = \beta = x$ and omit these indexes. For example, $F_{ij}^{\alpha\beta}(\mathbf{k}) \Rightarrow F_{\text{nn}}^{xx}(\mathbf{k}) \Rightarrow F(\mathbf{k})$.

More compact, but less detailed information on the statistics of turbulence is given by one-dimensional (1D) energy spectra $E(k)$ averaged over all directions of vector \mathbf{k} :

$$E_{\text{sp}}(k) = \frac{k^2}{(2\pi)^3} \int F(\mathbf{k}) d \cos \theta d\varphi, \quad (4a)$$

Here we used spherical coordinates, with polar and azimuth angles θ and φ . The polar angle is measured from the direction of \mathbf{U}_{ns} .

In the isotropic case $F(\mathbf{k}) = F(k)$, i.e., is independent of θ and φ . Thus

$$E_{\text{sp}}(k) = \frac{k^2}{2\pi^2} F(k), \quad \text{for spherical symmetry.} \quad (4b)$$

Some information about possible anisotropy of the 2nd-order statistics of turbulence can be obtained by comparison of the 1D (spherically averaged) functions $E_{\text{sp}}(k)$, Eq.(4c) with the 1D functions $E_{xy}(k_z)$, $E_{zx}(k_y)$, and $E_{yz}(k_x)$, averaged over xy , zx , and yz planes. These functions depend only on the projections of \mathbf{k} orthogonal to the corresponding planes. Understanding $F(\mathbf{k})$ in the

1	2	3	4	5	6	7	8	9	10	11	12	13	14	15	16
T ,	$\frac{\rho_n}{\rho}$	α	Q ,	U_n ,	U_{ns} ,	\mathcal{L} ,	Re_n	k_\times	k_ν	k_*	k_ℓ	$n+1$	$\langle m \rangle_{10}$	m_C	m_F
K			$\frac{\text{mW}}{\text{cm}^2}$	$\frac{\text{cm}}{\text{s}}$	$\frac{\text{cm}}{\text{s}}$	$\frac{1}{\text{cm}^2}$		$\frac{1}{\text{cm}}$	$\frac{1}{\text{cm}}$	$\frac{1}{\text{cm}}$	$\frac{1}{\text{cm}}$				
1.65	0.11	0.11	150	1.87	2.32	86300	37.9	37.2	149	294	1846	1.89	2.00	1.7	3.0
			200	2.23	2.76	16200	46.2	58.8	224	402	2529	2.14	2.10	1.8	3.0
			300	3.27	4.04	38200	84.9	94.5	354	618	3883	2.18	2.20	1.9	2.9
1.85	0.19	0.18	200	1.18	1.85	81100	53.2	43.8	249	322	1788	1.88	1.88	1.7	3.0
			300	1.78	2.80	19800	94.2	70.1	539	502	2796	2.23	1.95	1.8	2.8
			497	3.03	4.76	58500	165	123	755	863	4806	2.35	2.20	1.9	2.8
2.00	0.55	0.28	233	0.86	1.92	14100	84.7	73.3	455	418	2359	2.3	2.20	1.7	3.0
			386	1.34	3.00	47300	131	158	690	765	4321	2.31	2.30	1.9	2.8
			586	2.09	4.67	112000	223	240	1102	1178	6650	2.36	2.30	2.2	3.0
2.10	0.74	0.48	200	0.57	2.20	37300	107	170	588	612	3837	2.30	2.25	1.7	2.9
			300	0.88	3.40	89800	159	264	958	951	5951	2.30	2.30	2.1	3.0
			350	0.99	3.83	114000	211	298	1142	1071	6705	2.30	2.35	2.2	3.0

TABLE I: Columns ## 1-3 – The temperature and temperature-dependent material parameters of ^4He ; Columns ## 4-7: the experimental parameters of the flow. Column # 8: the estimates of the normal-fluid Reynolds number, Eq. (14b); Columns # 7-12: the estimates of the characteristic wavenumbers: k_\times , k_ν , k_* and k_ℓ , Sec. III B. Column #13 – the estimates of the scaling exponents of the energy spectra via apparent scaling exponents of $S_2(Y)$. Column #14 – the mean-over-decade scaling exponents of the energy spectra $\langle m \rangle_{10}$. Columns # 15 and # 16: the apparent scaling exponents of the energy spectra in the cascade dominated subinterval, m_C and in the mutual-friction dominated subinterval, m_F .

Cartesian coordinates as $F(k_x, k_y, k_z)$, we define

$$\begin{aligned}
E_{xy}(k_z) &= \int F(k_x, k_y, k_z) \frac{dk_x dk_y}{4\pi^2}, \\
E_{zx}(k_y) &= \int F(k_x, k_y, k_z) \frac{dk_x dk_z}{4\pi^2}, \\
E_{yz}(k_x) &= \int F(k_x, k_y, k_z) \frac{dk_y dk_z}{4\pi^2}.
\end{aligned} \tag{4c}$$

The total kinetic energy E of the system can be found by respective integration:

$$E = \int E_{\text{sp}}(k) \frac{dk}{2\pi} = \int E_{xy}(k_z) \frac{dk_z}{2\pi} = \dots \tag{5}$$

In the case of spherical symmetry, all four 1D functions Eq. (4b) and Eq. (4c) are proportional to each other (i.e., differ only by numerical prefactors). If the angular distribution of energy is not symmetric, the behavior of different energy spectra will differ.

B. A new way of statistical analysis of the visualization data

As we mentioned, the visualization technique allows one to measure the streamwise velocity across a channel as a function of a wall-normal coordinate y for fixed values of the time t_0 and the spanwise and streamwise positions z_0 and x_0 :

$$u(y) \equiv u_x(x_0, y, z_0, t_0). \tag{6}$$

For simplicity, we choose $t_0 = 0$ and $z_0 = x_0 = 0$, i.e., $u_x(0, y, 0, 0)$.

So far, the way to statistically analyze the data, i.e., Eq. (6), was to find the velocity differences $\Delta u_x(Y, y, t)$ defined in Eq. (1b) and calculate the structure functions $S_n(Y)$ using Eqs. (1a) and (2). The theoretical analysis of homogeneous turbulence is traditionally done in the Fourier space, where different Fourier components are statistically independent: $\langle v^\alpha(\mathbf{k})v^\beta(\mathbf{k}') \rangle = 0$, if $\mathbf{k} \neq \mathbf{k}'$. We will demonstrate in this paper that similar approach (in the k_y -space) to the data analysis of the visualization data allows one to get additional information on the statistics of counterflow turbulence that is hidden in the approach based on $S_2(\delta)$.

To this end, we define a 1D-Fourier transform, $v(k_y)$ similar to its 3D-version Eq. (3b):

$$v(k_y) = \int_{-D/2}^{D/2} u(y) \exp(ik_y y) dy. \tag{7a}$$

Here $y = 0$ is the position of the centerline and D is the channel width. Similarly to Eq. (3a), we define next the 1D energy spectrum

$$2\pi \delta(k_y + k'_y) E(k_y) = \langle v(k_y)v(k'_y) \rangle, \tag{7b}$$

which is nothing but $E_{xz}(k_y)$ defined by Eq. (4c). To see this, notice that integration over $dk_x/(2\pi)$ and $dk_z/(2\pi)$ in Eq. (4c), according to Eq. (3c), results in $u_i(x = 0, y, z = 0)$.

Our expectation is that $v(k_y)$ (and respectively $E(k_y)$) better separates turbulent fluctuations with different

scales than $\Delta u(Y, y)$ (and respectively $S_2(Y)$). To see this, one may consider relation between $E(k_y)$ and $S_2(Y)$. Using inverse Fourier transform of Eq. (7a):

$$u(y) = \int v(k_y) \exp(-ik_y y) dy, \quad (7c)$$

in the definition of $S_2(Y)$ (i.e., Eq. (1a)) and applying Eq. (7b), one gets:

$$S_2(Y) = \frac{2}{\pi} \int \sin^2\left(\frac{k_y Y}{2}\right) E_{xz}(k_y) dk_y. \quad (7d)$$

If this integral converges, it is dominated by the range $k \sim 1/Y$. Therefore, for the infinite extend of the inertial interval $S_2(Y) \sim F_2(1/Y)Y^{-1}$. For example, if $F(k) \propto k^{-m}$, then $S_2(Y) \propto Y^n$ with $n = m - 1$. It is important to note that integral Eq. (7d) has also contribution from a wide range of k around $1/Y$. Therefore, in a realistic situation with a finite extend of available k -space, the relation between $F_n(k_y)$ and $S_n(Y)$ is not so simple.

In any case, one expects, as we will demonstrate in this paper, that direct measurement of the *integrand* $E_{xz}(k_y)$ gives more detailed information about the statistics of counterflow turbulence than the measurements of the *integral* (Eq. (7d)) for $S_2(Y)$.

C. Overview of the theory of counterflow turbulence

Analytical theory of counterflow superfluid turbulence, developed in Ref. ¹⁷, describes the energy spectra of the normal-fluid and superfluid components of superfluid ⁴He at scales r exceeding intervortex distance $\ell = 1/\sqrt{\mathcal{L}}$, where \mathcal{L} is the vortex density, i.e., total length of vortex lines per unit volume. The theory is based on the gradually-damped version²⁰ of the coarse-grained Hall-Vinen-Bekarevich-Khalatnikov(HVBK) equations, generalized in Ref. ²¹ for the counterflow turbulence. These equations have a form of two Navier-Stokes equations for the turbulent velocity fluctuations $\mathbf{u}_n(\mathbf{r}, t)$ and $\mathbf{u}_s(\mathbf{r}, t)$, coupled by a simplified version of the mutual friction force²²

$$\mathbf{f}_{\text{ns}} \simeq \Omega_s [\mathbf{u}_n(\mathbf{r}, t) - \mathbf{u}_s(\mathbf{r}, t)], \quad \Omega_s = \alpha(T)\kappa\mathcal{L}. \quad (8)$$

Here $\alpha(T)$ is the temperature dependent parameter of the mutual friction, listed in Table I, column # 3.

These equations served as a starting point for derivation of the stationary balance equations for the 1D energy spectra $E_n(k)$ and $E_s(k)$ of the normal and superfluid components

$$\frac{d\varepsilon_j(k)}{dk} = \Omega_j [E_{\text{ns}}(k) - E_j(k)] - 2\nu_j k^2 E_j(k), \quad (9)$$

using simplifying assumption of the spatial homogeneity and isotropy of the counterflow turbulence statistics. Here $\varepsilon_j(k)$ is the energy flux over scales $1/k$ in

the normal-fluid ($j = n$) and superfluid ($j = s$) velocity components, $\Omega_n = \Omega_s \rho_s / \rho_n$, ν_n is the normal-fluid kinematic viscosity (normalized by the ρ_n), and ν_s is the Vinen's effective superfluid viscosity⁵. The viscous-like energy sink term was added to HVBK equations in Ref. ²⁰ to account for the energy dissipation at the intervortex scale ℓ due to vortex reconnections, the energy transfer to Kelvin waves, and similar effects. In Eq. (9), $E_n(k)$ and $E_s(k)$ are the 1D spherically averaged energy spectra [cf. Eq. (4a)] of the normal-fluid and superfluid subsystems and the cross-correlation function $E_{\text{ns}}(k)$ is related similarly to $F_{\text{ns}}(\mathbf{k})$.

Eqs. (9) are exact (in the framework of HVBK equations), but not closed. To make them practically useful, the closure approximations for $\varepsilon_j(k)$ and for $E_j(k)$ in the terms of $E_j(k)$ were used.

The role of long-range (in the k -space) energy-transfer terms was analyzed¹⁷, based on the integral closure for $\varepsilon(k)$ ²³, and a new self-consistent closure was suggested:

$$\varepsilon(k) = C(k)k^{5/2}E^{3/2}(k), \quad C(k) = \frac{4C}{3[3 - m(k)]}. \quad (10a)$$

in which $m(k)$ should be understood as a local scaling exponent of $E(k)$:

$$m(k) = \frac{d \ln E(k)}{d \ln(k)}, \quad (10b)$$

and the prefactor $C(k)$ is chosen to reproduce the Kolmogorov constant C for the K41 scaling exponent $m(k) = 5/3$.

To complete the closure of Eqs. (9), the closure²¹ for the cross-correlation function E_{ns} was adopted. In a simplified form, suitable for conditions of the visualization experiments^{13,14}, it reads:

$$E_{\text{ns}}(k) = D(k)E_{\text{ns}}^{(0)}(k), \quad D(k) = \frac{\arctan[\xi(k)]}{\xi(k)}, \quad (11a)$$

$$\xi(k) = \frac{k}{k_\times}, \quad k_\times = \frac{\Omega_{\text{ns}}}{U_{\text{ns}}}, \quad \Omega_{\text{ns}} = \Omega_n + \Omega_s = \alpha\kappa\mathcal{L}\frac{\rho}{\rho_n}, \quad (11b)$$

$$E_{\text{ns}}^{(0)}(k) = [\rho_n E_n(k) + \rho_s E_s(k)] / \rho. \quad (11c)$$

Here $D(k)$ is the U_{ns} -dependent decoupling function and $E_n(k)$ and $E_s(k)$ are the U_{ns} -dependent energy spectra, found self-consistently by solving Eqs. (9) with $E_{\text{ns}}(k)$ given by Eqs. (11).

Further simplification of the balance Eqs. (9), (10), and (11) for the experimental conditions, results in decoupled balance equations for the normal-fluid and the superfluid energy spectra:

$$C(k) \frac{d}{dk} k^{5/2} E_j^{3/2}(k) = E_j(k) \{ \Omega_j [D(k) - 1] - 2\nu_j k^2 \}, \quad (12)$$

in which $C(k)$ and $D(k)$ are given by Eqs. (10a) and (11a). The solutions of these equations are compared with the experimental spectra in Figs. 3.

To summarize this overview, note that analytical theory¹⁷ describes the main features of the large scale normal-fluid energy spectra of counterflow turbulence, observed in the visualization experiments, although it does not account for the inhomogeneity and anisotropy of the flow.

III. EXPERIMENTAL RESULTS AND THEIR ANALYSIS

In this section we analyze the experimental data of the normal-fluid turbulent velocity fluctuations $u(y)$, obtained for $T = 1.65$ K, 1.85 K, 2.00 K, and 2.10 K with three values of heat fluxes Q at each temperature. Main parameters of these experiments are given in Table I. This table also collects the values of important characteristic wavenumbers, estimated below in Sec. III B. The second-order statistics (i.e., the structure functions and the spectra $E_{zx}(k_y)$) are discussed in Sec. III C and the higher-order statistics of the structure functions in Sec. III E.

A. Experimental techniques

The experimental apparatus is identical with that described in Refs.^{13,14}. A stainless steel channel of 9.5 mm square cross section with a total length of 300 mm is attached to a pumped helium bath whose temperature can be controlled within 0.1 mK by regulating the vapor pressure. A planar heater (around 400 Ω) at the lower end of the channel was used to drive a thermal counterflow. When the heat flux is sufficiently large, both the superfluid and the normal fluid components can become turbulent. To probe the normal fluid turbulence, our recently developed He₂* molecular tracer-line tracking technique²⁴ was adopted. A 35-fs pulsed laser with a repetition rate of 5 kHz and a pulse energy of about 60 μ J was focused into the channel to produce a thin line of He₂* molecular tracers. This tracer line can be driven to produce 640 nm fluorescent light by a pulse train from an imaging laser at 905 nm (i.e., 5-6 pulses at a repetition rate of 500 Hz). The fluorescence was captured by an intensified CCD (ICCD) camera, mounted perpendicular to both the flow direction and the laser beam path, to produce the images of the tracer line. In a typical experiment, a straight baseline image is acquired to serve as a reference. Then, the heater is turned on for at least 20 s so that a fully developed counterflow can establish in the channel. After that, we produce a tracer line and let the tracer line move with the normal fluid by a drift time Δt before the drifted line is imaged.

In order to extract quantitative velocity field information, the center location of every line segment needs to be accurately determined. In our previous research^{13,14}, a simple Gaussian fit method was adopted. First, the image of a tracer line was cut into many small segments (i.e., typically 40-60 segments). Then, the fluorescence

intensity profile of each line segment was fit by a Gaussian function such that both the center location and the width of the line segment can be determined. The streamwise velocity of the normal fluid at position y can be calculated as the displacement of the line segment divided by the drift time Δt . This method works well only when the tracer-line image has good quality and high signal-to-noise ratio. However, as the normal fluid velocity increases, some line segments can distort and smear, which can result in significant uncertainty in locating the center of these segments using the Gaussian fit method. In this research, we utilized a more sophisticated approach, which is based on the algorithm proposed by Pulkkinen *et al.* for finding curvilinear structures in noisy data²⁵. There are two steps involved in the image analysis. First, a tracer-line image is noise-filtered based on the intensity of bright pixels using numerically inexpensive nearest-neighbors searches. The basic idea is to remove those bright pixels that are surrounded all by dark pixels and hence are more likely created due to instrument or environmental noises²⁶. Subsequently, the algorithm of Ref.²⁵ is applied to determine the ridge line of the entire fluorescence intensity profile. The displacement of the ridge line then allows us to calculate the streamwise normal-fluid velocity regardless of the bad quality of some local line segments.

Based on the obtained streamwise normal-fluid velocity $u_x(y)$, we can evaluate the velocity difference $\Delta u_x(Y, y) = u_x(y+Y) - u_x(y)$, between two line segments that are separated by a distance Y . Then, the transverse structure functions of the normal fluid turbulence can be easily computed as $S_n(Y) = \langle |\Delta u_y(y, Y)|^n \rangle$, where the angle brackets $\langle \dots \rangle$ denote an ensemble average over all the images obtained under the same experimental conditions (typically 30-100 images). The calculated structure function profiles are found to be insensitive to the reference location y . The 1D-energy spectra, averaged over x - z plane and parallel to the channel wall can also be determined. In Fig. 1, we show the obtained structure function and energy spectra curves at various temperatures and heat fluxes. It should be noted that the results for separation distance Y smaller than the thickness of the tracer line (i.e., about 100-200 μ m) can have large uncertainties.

B. Estimates of the cross-over wavenumbers

1. Decoupling wavenumber k_\times

According to Ref.²¹, the decoupling wavenumber k_\times , for which the decoupling function $D(k) = \frac{1}{2}$, is estimated as

$$k_\times \simeq 2\Omega_{\text{ns}}/U_{\text{ns}} \simeq \kappa\mathcal{L}/U_{\text{ns}}. \quad (13)$$

For typical values $\mathcal{L} \simeq 10^5$ cm⁻², $U_{\text{ns}} \simeq 1$ cm/s and with $\kappa \simeq 10^{-3}$ cm²/s, this gives $k_\times \simeq 100$ cm⁻¹. The particu-

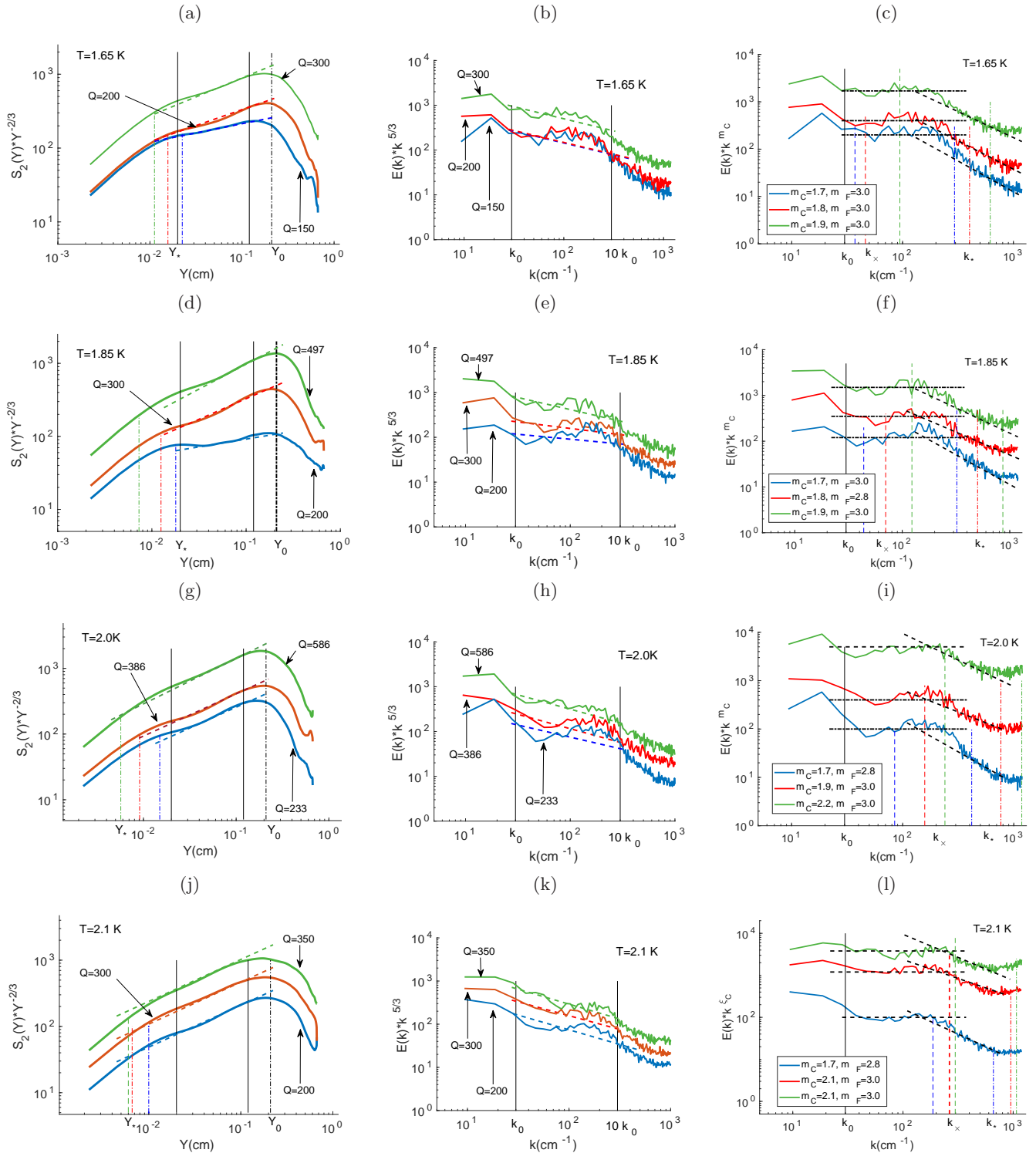


FIG. 1: The second-order statistics for different T and heat fluxes Q . The figures in the rows (top to down) correspond to $T = 1.65$ K, 1.85 K, 2.0 K, and 2.1 K, respectively. Left column: The second-order structure functions, compensated by K41 scaling, $Y^{-2/3}S_2(Y)$. The colored thin straight lines denote fits with exponents n (cf. Table I, Column #13). The fitting range (according to Ref. ¹³) is denoted by black vertical thin lines. The black vertical dot-dashed line marks the outer scale of turbulence, denoted as Y_0 . The colored vertical dot-dashed line (collectively marked as Y_*) denote the scales, corresponding to the respective crossover wavenumbers k_* . Middle column: the energy spectra compensated by K41 scaling $k^{5/3}E(k)$. Dashed lines of matching colors denote fits $E(k) \propto k^{-m}$ in the wavenumber interval $k \in [k_0, 10k_0]$, shown by black vertical lines. Right column: the energy spectra, compensated by an individual scaling, $k^{m_c}E(k)$, found by fitting each spectrum in the cascade-dominated range. The compensation is emphasized by horizontal dot-dashed lines. The fits of the mutual-friction dominated range, $E(k) \propto k^{-m_F}$ are shown by black dashed lines. The vertical lines, corresponding to the crossover wavenumbers k_* (dashed lines) and k_x (dot-dashed lines), are marked in the same color as the corresponding spectra. The legend indicate the scaling exponents m_c for the cascade-dominated range and m_F for the mutual-friction dominated range. The outer scale of turbulence $k_0 = 2\pi/Y_0$ is marked as a black solid thin line. Different heat fluxes Q (in mW/cm²) are color coded: green lines denote the largest Q , red lines – intermediate Q and blue lines – the smallest Q . The color code is the same in all panels.

lar values of k_\times for each of the 12 experimental sets are presented in Table I, column #9 .

2. Viscous wavenumber k_ν

The viscous wavenumber k_ν , for which the viscous damping becomes comparable with the energy transfer over scales, can be estimated by comparison of the viscous damping frequency νk^2 with the eddy-turnover frequency $\sqrt{k^3 E(k)}$:

$$k_\nu \simeq E(k_\nu)/\nu^2 . \quad (14a)$$

Using K41-estimate for the energy spectrum $E_{K41}(k) \simeq u_\tau^2 k_0^{2/3} k^{-5/3}$ we get

$$\frac{k_\nu}{k_0} \simeq \left[\frac{E(k_\nu)}{E_{K41}(k_\nu)} \right]^{3/8} \text{Re}^{3/4}, \quad \text{Re} = \frac{u_\tau}{k_0 \nu} . \quad (14b)$$

Here $k_0 \simeq 30 \text{ cm}^{-1}$, estimated in Ref. ¹³ from the behavior of $S_2(Y)$. Our estimates of k_ν are given in Table I, column #10.

Eq.(14b) is a generalization of the well known K41 relationship $k_\nu \simeq k_0 \text{Re}^{3/4}$ for the spectra that differ significantly from the K41 scaling $E_{K41}(k) \propto k^{-5/3}$.

3. Mutual friction – viscous crossover wavenumber k_*

We know that the characteristic frequency, responsible for the rate of energy dissipation by mutual friction in the normal fluid component is $\alpha \frac{\rho_s}{\rho_n} \kappa \mathcal{L}$, while the corresponding frequency for the viscous dissipation is $\nu_n k^2$. Comparing these two frequencies, one find a crossover wave number k_* for which the efficiency of these two dissipation mechanisms is equal:

$$k_* = \sqrt{\alpha \frac{\rho_s}{\rho_n} \frac{\kappa}{\nu_n} \mathcal{L}} . \quad (15)$$

Substituting the particular temperature dependent values of α , ρ_n and ν_n , we get the values shown in Table I, rows #11. As we see, for $T = 1.65 \text{ K}$ and $T = 2.10 \text{ K}$ $k_* \approx 1.0 \sqrt{\mathcal{L}}$, while for $T = 1.85 \text{ K}$ and $T = 2.00 \text{ K}$ $k_* \approx 1.1 \sqrt{\mathcal{L}}$. This is smaller than the wavenumber

$$k_\ell \approx 2\pi \sqrt{\mathcal{L}}, \quad (16)$$

(cf. Table I, column #12), that separates the quasi-classical and ultra-quantum regimes of superfluid turbulence.

C. Second-order statistics of counterflow turbulence

Fig.1 summarizes the second order statistics of the velocity fluctuations for different temperatures and flow

parameters. Both the structure functions (left column) and the 1D energy spectra, are compensated by the K41 scaling: $Y^{2/3} S_2(Y)$, $k_y^{5/3} E_{xz}(k_y)$. In the right column, we plot the energy spectra compensated in the cascade-dominated range, see below.

1. Second-order structure functions

The structure functions in the counterflow share similarity with the velocity structure functions in the classical hydrodynamic turbulence. The expected inertial interval of scales $\delta_{\min} \approx 0.02 \text{ cm}$ to $\delta_{\max} \approx 0.2 \text{ cm}$ is marked by black thin vertical lines and correspond to that in Ref. ¹³. Clearly, the structure functions are steeper than their classical counterparts. The apparent scaling behavior in this interval of scales may be characterized by exponents n . These exponents were found in Ref. ¹³ and are reproduced in Table I, column #13. The values of n for $T = 2.1 \text{ K}$ are slightly larger than in Ref. ¹³, likely due to the improved image analysis and the fitting procedure. Note that the values of n vary widely, depending on the flow parameters: the temperature and the heat flux.

The dot-dashed vertical lines, colored as the structure functions and collectively marked Y_* , denote the scale that delineate the ranges of dominance of two dissipative mechanisms: the mutual friction (for $Y > Y_*$) and the viscous dissipation (for $Y < Y_*$).

We should also note that simple analysis of Eq.(7d) shows that the small scale behavior $S_2(Y) \propto Y^2$ appears if the energy spectrum $E(k)$ decays as k^{-3} or faster (including the exponential decay). Therefore, the apparent Y^2 -scaling cannot be uniquely connected with the viscous dissipation of turbulent kinetic energy, as in the classical turbulence. Moreover, the asymptotic slope $S_2(Y) \propto Y^2$ at $Y \lesssim Y_*$ is not reached in our experiments due the limited spatial resolution (cf. Fig. 4a).

2. Energy spectra of counterflow turbulence

One-dimensional energy spectra, compensated by K41 scaling $k^{5/3} E(k)$, are shown in Figs.1, middle column. We can easily identify several k -ranges with different k -dependence of the spectra. The small wavenumber ($k \lesssim k_0$) behavior is clearly different from the rest of the spectrum. A relatively short part of the spectra is close to compensation by K41 while remaining steeper. The large- k part of the spectra has a much larger slope, extending over all remaining interval of scales. We will now try to relate between these different types of behavior and various crossover wavenumbers introduced in Sec. III B.

a. Energy-containing interval. The outer scale of turbulence, $k_0 \simeq 30 \text{ cm}^{-1}$, was taken according to Ref. ¹³, where it was estimated as $2\pi/r_0$ with $r_0 \simeq 0.2 \text{ cm}$ close to the maximum of the structure functions. The positions of k_0 are marked in Fig.1, middle and right

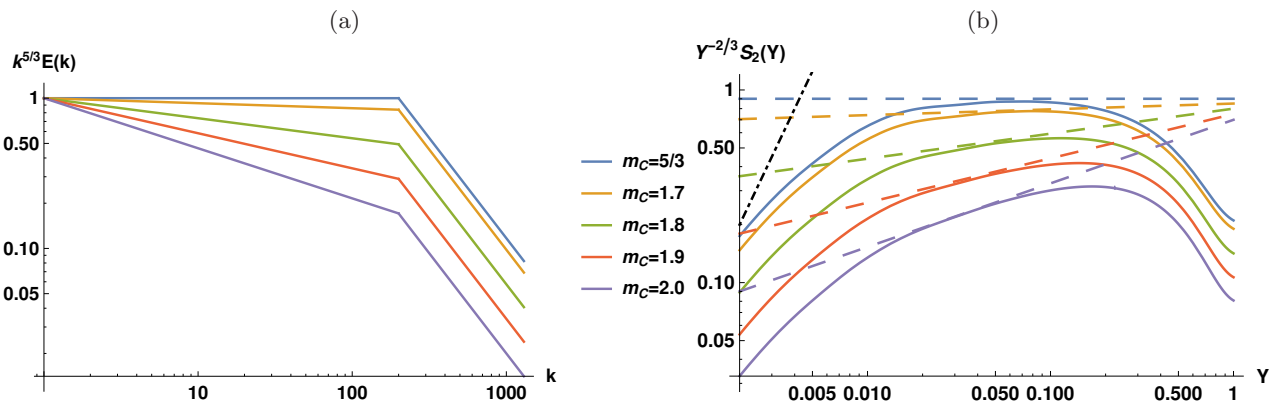


FIG. 2: (a) Piecewise-linear model of the energy spectra $E(k) \propto k^{-m_C}$ for $k < k_\times$ in the cascade-dominated interval and $E(k) \propto k^{-m_F}$, $m_F = 3$ in the mutual friction-dominated and (b) structure functions $S_2(Y)$, computed using Eq. (7d). The dashed lines of the matching colors correspond to Y^{m_C-1} . The black dot-dashed line corresponds to Y^2 .

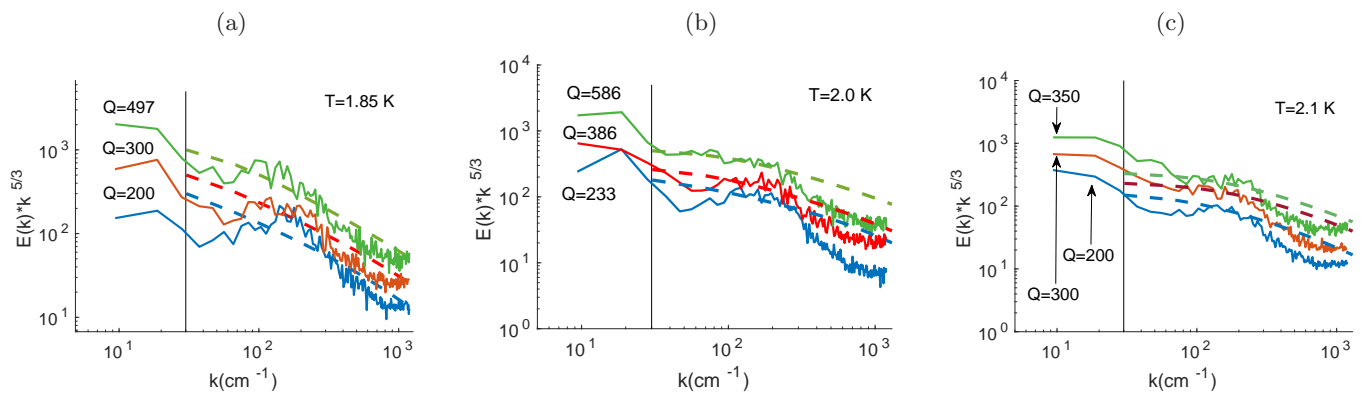


FIG. 3: Comparison of the experimental compensated energy spectra $k^{5/3}E(k)$ with the theoretical predictions¹⁷ (dashed lines) for different temperatures T K and heat fluxes Q (in mW/s^2). Vertical solid lines denote the outer scale k_0 .

columns, by vertical black thin solid lines. The range $k \lesssim k_0$ can be interpreted as an energy-containing interval, where energy is pumped into the system due to instabilities of mean flow in the channel and in which the most of the flow energy is localized. As we see, this value corresponds well to a boundary between the large-scale behavior and the inertial-like scaling behavior of the spectra for large heat fluxes, while for low heat fluxes and low temperature, the energy-containing interval seems to extend to higher wavenumbers.

b. Cascade-dominated interval. Next characteristic scale, k_\times (cf. Table I, Column #9) estimates the wavenumber for which the decoupling function $D(k_\times) = \frac{1}{2}$. For $k \lesssim k_\times$, $D(k) > \frac{1}{2}$, and the energy dissipation by the mutual friction is relatively weak. In this k -range the main mechanism, responsible for the energy transfer over scales is the Richardson-Kolmogorov energy cascade, similar to that in classical turbulence. Nevertheless the energy dissipation by the mutual friction cannot be fully ignored. Therefore the energy spectra in this range of scales are steeper than the K41 scaling, as is clearly seen in Figs. 1, middle column. All these motivate us to

name the wavenumber range $k_0 \lesssim k \lesssim k_\times$ as *cascade-dominated interval*.

It was suggested in Ref. 17 to characterize the apparent scaling of the otherwise not-scale-invariant spectra by calculation of a mean exponent over some interval of scales. The theoretical mean exponents over a first decade $\langle m \rangle_{10}$ were found to agree with the experimental exponents¹³ of the structure functions¹⁷. We calculated the mean exponents over a k -range $k \in [30 - 300]$ (a decade in k/k_0) and collected them in Table I, column #14. These values are close to $n + 1$, where n is apparent scaling exponent of $S_2(Y) \propto Y^n$, defined by Eq. (7d). This means that the idea to estimate $\langle m \rangle_{10}$ via $n + 1$ indeed works reasonably well. The corresponding fits are shown in Fig. 1 middle column as dashed colored lines. However, although the values of the mean exponents agree with the scaling of the structure functions, the actual scaling of the spectra is different.

To estimate the apparent scaling exponents m_C of the energy spectra $E(k) \propto k^{-m_C}$ in the cascade-dominated interval, we plot the experimental spectra, compensated by k^{m_C} and choose the value of m_C so as to maximize

the k -range where $k^{m_C} E(k) \approx \text{const}$. The resulting plots are shown in Fig. 1, right column, where the crossover scales k_\times are shown by vertical dashed colored lines. It is remarkable that, except for the low heat fluxes at $T = 1.65$ and 1.85 K, the cross-over between different scaling regimes of the energy spectra coincide well with k_\times .

c. Mutual-friction dominated interval. For $k \gtrsim k_\times$, where the decoupling function is small and mutual friction becomes important in the energy balance¹⁷, the slope of the energy spectra increases significantly from $m_C \approx 2.0 \pm 0.2$ to $m_F \approx 2.9 \pm 0.1$. The transition between two types of behavior is not sharp, especially for low heat fluxes, but clearly visible.

The power-law-like behavior $E(k) \propto k^{-m_F}$ qualitatively differs from the exponential decay of $E(k)$, typical for the viscous interval of k in the classical hydrodynamic turbulence. Therefore, we consider this behavior as an evidence that for $k \gtrsim k_\times$ the main mechanism of the energy dissipation is the mutual friction. Upper limits of the mutual-friction dominated interval k_* , are shown in Fig. 1, right column, by vertical dot-dashed lines of the corresponding colors. As a rule, the values of k_* are about or above the largest available values of k . This means that the viscous interval of wavenumbers is beyond our spectral resolution. The corresponding Y_* are shown in the Fig. 1, left column, and are mostly smaller than the implied boundary between the inertial and viscous behavior¹³ (i.e., black vertical thin solid lines). Therefore, only at the smallest scales, the viscous dissipation becomes important, but it is still not dominant as we show below.

3. More about connection between $S_2(Y)$ and $E(k)$

To clarify the relation between the energy spectra in a finite k -range and the structure functions, we plot in Fig. 2 (a) a piecewise-linear model of the energy spectra, consisting of $E(k) = k^{-m_C}$ in the cascade dominated interval $k_0 < k < k_\times$, continuously connected with the $E(k) \propto k^{-m_F}$ part in the mutual-friction dominated interval $k_\times < k < k_*$. We used the typical values of m_C , and the same values of $m_F = 3.0$, $k_\times = 200 \text{ cm}^{-1}$, and $k_* = 1300$ for all spectra. For simplicity, we adopt for the energy containing interval the same behavior $E(k) = k^{-m_C}$ as in the cascade dominated interval. The structure functions, computed using Eq. (7d), are shown in Fig. 2 (b) together with the expected slope $S_2(Y) \propto Y^n$ with $n = m_C - 1$, shown by the dashed lines. As we see, the actual range of scales, over which the original scaling is recovered, is very narrow.

The slope $S_2(Y) \propto Y^2$, typical for viscous exponential decay of $E(k)$ in the classical hydrodynamic turbulence, and $E(k) \propto k^{-3}$, typical for the mutual friction dominated interval in counterflow turbulence, are shown by black dot-dashed line. As expected, for the finite scaling interval of a modest extent, the resulting Y -dependence of $S_2(Y)$ demonstrates very smooth transition between

these regimes and does not reach the genuine asymptotic behavior $S_2(Y) \propto Y^2$.

D. Comparison of analytically predicted and experimental energy spectra

It is instructive to compare directly the experimental spectra with the spectra predicted by theory¹⁷. Remind that the theory does not describe the largest scales motion in the energy-containing interval (for $k < k_0$) and has the energy influx for $k = k_0$ (or the boundary condition $E_0 = E^{\text{th}}(k_0)$) as an external parameter of the theory.

The theory was developed for an idealized situation of fully-developed, space homogeneous turbulence. Naturally, the real physical situation in the experiments (i.e., wall-bounded, space-inhomogeneous channel flow for relatively low Reynolds numbers) is more complicated than assumed by the theory. Therefore, the comparison is meaningful only for the experiment with relevant flow conditions. In our case, we may take the $\text{Re}_n > 100$ as a tentative criterion for the well-developed turbulence in the channel. This leaves out the low temperature data ($T = 1.65$ K), as well as lowest heat fluxes for $T = 1.85$ and 2.0 K. However we keep for completeness all the data for $T = 1.85$ K and 2.0 K.

In Figs. 3 we compare the experimental (K41-compensated) energy spectra for $T = 1.85$ K, 2.0 K and 2.1 K (plotted as solid colored lines) with the predicted energy spectra (denoted by dashed lines of the same color), calculated for the same temperatures and the same heat fluxes. The theoretical spectra were made dimensional and $E^{\text{th}}(k_0)$ was taken to ensure overlap in the cascade-dominated k -range. For high heat fluxes, these values agree well with $E^{\text{exp}}(k_0)$.

The immediate observation is a qualitative agreement between the experimental and theoretical spectra over large range of wavenumbers, covering most of the cascade-dominated range. The deviations are mostly limited to the spectra with the lowest heat fluxes for $T = 2.0$ K and $T = 2.1$ K. At $T = 1.85$ K, the agreement is recovered for wavenumbers larger than k_0 , which may indicate that the turbulence in these experiments is not yet fully developed and the outer scale is smaller than expected.

As mentioned above, the overall suppression of the spectra compared to the classical behavior is well captured by the mean scaling exponents $\langle m \rangle_{10}$, cf. Table I, column #14.

On the other hand, the theory does not describe the sharp drop of the spectra in the mutual-friction dominated k -range, demonstrating only smooth decrease of the current slope $m(k)$ of the spectra for large k . A possible reason is that the theory¹⁷ does not take into account the energy exchange between components, that is most efficient in this range of scale. Other flow conditions, which are not accounted for by the

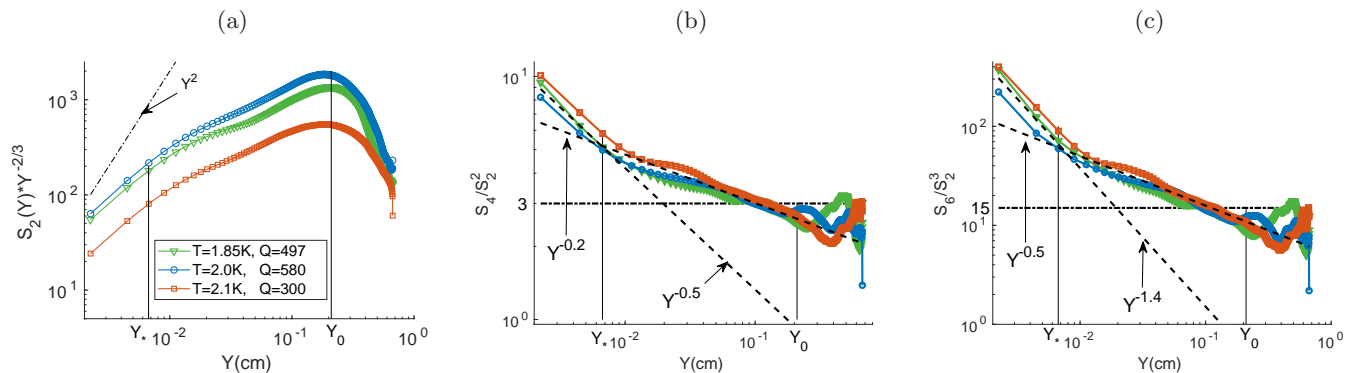


FIG. 4: Second- and higher-order statistics at different temperatures. The flow parameters are shown in the legend of panel (a). Panel (a): the structure functions $S_2(Y)$. Dot-dashed black line denotes the asymptotic viscous behavior for $S_2(Y) \propto Y^2$. Panel (b): Flatness $F_4(Y) = S_4(Y)/S_2^2(Y)$. Panel (c): Hyper-flatness $F_6(Y) = S_6(Y)/S_2^3(Y)$. The horizontal dot-dashed lines in panels (b) and (c) denote the Gaussian values of $F_4(Y)$ and $F_6(Y)$. The approximate Y -dependencies of the flatness and hyperflatness for $Y \gtrsim Y_*$ are shown by dashed lines, marked $Y^{-0.2}$ and $Y^{-0.5}$, respectively. These values are slightly larger than typical for the classical hydrodynamic turbulence, i.e., $\delta^{-0.14}$ and $\delta^{-0.38}$ in Ref. 27. However for $Y \lesssim Y_*$, the effective slopes of $F_4(Y)$ and $F_6(Y)$ strongly increase and become much larger than the classical values, see the dashed lines, marked as $Y^{-0.5}$ and $Y^{-1.4}$, respectively. The vertical thin lines in all panels denote positions of the outer scale Y_0 and the crossover scale Y_* .

theory, may contribute to this discrepancy. Also the experimental data in the high k regime may not be very reliable indeed. This is because the corresponding separation scale is comparable or even smaller than the width of the tracer line, which leads to large uncertainty.

E. Flatness, hyper-flatness and intermittency

To analyze higher order statistics and possible intermittency effects, we select one example at each temperature, having similar Y_* , and plot in Fig. 4 the structure functions $Y^{-2/3}S_2(Y)$, the flatness $F_4(Y) = S_4(Y)/S_2^2(Y)$, and the hyper-flatness $F_6(Y) = S_6(Y)/S_2^3(Y)$.

In all panels, we mark the positions of the outer scale of turbulence Y_0 and the crossover scale Y_* . As is clearly seen in Fig. 4a, the asymptotic behavior Y^2 is not reached with our spatial resolution. However, Y_* delineates different types of behavior of the $S_2(Y)$. These different regimes are even better exhibited by flatness and hyper-flatness in Figs. 4(b) and (c).

Remind that for Gaussian statistics $F_4 = 3$ and $F_6 = 15$, shown in Figs. 4 (b) and (c) as horizontal dashed lines. Clearly, for large scales $Y \gtrsim Y_0$, $F_4(Y)$ and $F_6(Y)$ are close to the Gaussian values, indicating that the statistics of the turbulent velocity field in the energy-containing interval is indeed close to Gaussian. This is a common property of classical hydrodynamic turbulence, independent of the way of its excitation.

In a wide interval of scales $Y_* \lesssim Y \lesssim Y_0$, covering scales corresponding to both the cascade-dominated and mutual-friction dominated spectral ranges, both $F_4(Y)$ (panel(b)) and $F_6(Y)$ (panel(c)) have a power-law-like

behavior $F_n(Y) \propto Y^{-x_n^{(1)}}$, with exponents $x_4^{(1)} \simeq 0.20 \pm 0.02$ and $x_6^{(1)} \simeq 0.5 \pm 0.03$. To compare these exponents with their counterparts x_n^{HT} in the classical hydrodynamic turbulence, remind that $x_n^{\text{HT}} = \zeta_n^{\text{HT}} - n\zeta_2^{\text{HT}}/2$, where ζ_n^{HT} is the scaling exponent of the n -order structure function in classical hydrodynamic turbulence. With the most recent experimental values 27 $\zeta_2^{\text{HT}} \approx 0.72$, $\zeta_4^{\text{HT}} \approx 1.30$ and $\zeta_6^{\text{HT}} \approx 1.78$, this gives $x_4^{\text{HT}} \approx 0.14$ and $x_6^{\text{HT}} \approx 0.38$. We conclude that the values $x_{4,6}^{(1)}$ are moderately, but distinctly larger than ζ_n^{HT} . Notably, the structure functions and higher-order statistics is not sensitive to the peculiarities of the energy spectra, in particular to the existence of two significantly different scaling ranges.

However, at smaller scales $Y \lesssim Y_*$, the effective slopes of $F_4(Y)$ and $F_6(Y)$ increase dramatically. The estimates, shown in Figs. 4 (b) and (c), give $x_4^{(2)} \simeq 0.5 \pm 0.1$ and $x_6^{(2)} \simeq 1.4 \pm 0.1$ at these scales, which correspond to the dissipative range with mixed contributions of the mutual-friction and viscous dissipations. The statistics become very intermittent. The fact that we do not observe saturation of $F_4(Y)$ and $F_6(Y)$, typical for the viscous range in the classical turbulence, supports our conjecture that the viscous dissipation-dominant range is beyond our resolution.

IV. CONCLUSION

In this paper, we report a detailed analysis of the energy spectra, second- and high-order structure functions of velocity differences in the superfluid ^4He counterflow turbulence, measured in a wide range of temperatures and heat fluxes. In particular, we discover two

ranges of wavenumbers k_y with very different apparent exponents of the one-dimensional energy spectra in the cascade-dominated (for relatively small k_y) and the mutual friction-dominated subintervals, respectively. The general behavior of the experimental spectra $E_{xz}(k_y)$ in the cascade-dominated range agrees well with the predicted energy spectra in Ref. ¹⁷.

The analysis of the statistics of the high-order structure functions shows that in the energy-containing interval the statistics of counterflow turbulence is close to Gaussian, similar to the classical hydrodynamic turbulence. In the cascade- and mutual friction-dominated intervals we found some modest enhancement of intermittency with respect of its level in classical turbulence. However, at small scales (but not yet viscous scales), the intermittency becomes much stronger than that in the classical turbulence.

In conclusion, we should remind that the theory, developed in Ref. ¹⁷, does not describe the experimental observations reported here in all details. Besides the obvious reason of space inhomogeneity, especially important for modest available Reynolds numbers Re_n , there is one more possible reason for some disagreement even in the $Re_n \rightarrow \infty$ limit. This is the anisotropy of statistics of counterflow turbulence. Although we do not have yet experimental information how strong the anisotropy of

turbulent statistics is, this effect is definitely there due to presence of preferred \mathbf{U}_{ns} direction and strong dependence of the cross-correlation function $E_{ns}(\mathbf{k})$ (between the normal fluid and superfluid velocity components) on the angle between \mathbf{U}_{ns} and \mathbf{k} , predicted in Ref. ²¹. The study the effect of anisotropy on the statistics of counterflow turbulence is in our nearest agenda. Nevertheless, the reasonable agreement between our observations and the theory ¹⁷, is encouraging. In particular, the crossover scales between different regimes, predicted by the theory using macroscopic parameters of the flow, and clearly observed in the spectra and structure functions, makes us believe that what we know so far contains essential part of the basic physics of the problem.

Acknowledgments

S. B and W.G. acknowledge support from the National Science Foundation under Grant No. DMR-1807291. The experiment was conducted at the National High Magnetic Field Laboratory, which is supported by NSF Grant No. DMR-1644779 and the state of Florida. The authors would also like to acknowledge J. Gao for assistance in processing the experimental data.

-
- ¹ R. J. Donnelly and C. F. Barenghi, The Observed Properties of Liquid Helium at the Saturated Vapor Pressure, *J. Phys. Chem. Ref. Data* **27**, 1217 (1998).
- ² R. J. Donnelly, *Quantized Vortices in Helium II* (Cambridge 3 University Press, Cambridge, 1991).
- ³ *Quantized Vortex Dynamics and Superfluid Turbulence*, edited by C.F. Barenghi, R.J. Donnelly and W.F. Vinen, *Lecture Notes in Physics* **571** (Springer-Verlag, Berlin, 2001).
- ⁴ R. P. Feynman, Application of quantum mechanics to liquid helium, *Progress in Low Temperature Physics* **1**, 17 (1955).
- ⁵ W. F. Vinen and J. J. Niemela, Quantum Turbulence, *J. Low Temp. Phys.* **128**, 167 (2002).
- ⁶ H. E. Hall and W. F. Vinen, The rotation of liquid helium II. I. Experiments on the propagation of second sound in uniformly rotating helium II, *Proc. Roy. Soc. A* **238**, 204 (1956).
- ⁷ W. F. Vinen, Mutual friction in a heat current in liquid helium II I. Experiments on steady heat currents, *Proc. R. Soc.* **240**, 114 (1957); Mutual friction in a heat current in liquid helium II. II. Experiments on transient effects, **240**, 128 (1957); Mutual friction in a heat current in liquid helium II III. Theory of the mutual friction, **242**, 493 (1957); Mutual friction in a heat current in liquid helium. II. IV. Critical heat currents in wide channels, **243**, 400 (1958).
- ⁸ R. N. Hills and P. H. Roberts, Superfluid mechanics for a high density of vortex lines, *Arch. Rat. Mech. Anal.* **66**, 43 (1977).
- ⁹ L. Skrbek and K. R. Sreenivasan, in *Ten Chapters in Turbulence*, edited by P. A. Davidson, Y. Kaneda, and K. R. Sreenivasan (Cambridge University Press, Cambridge, 2013), pp. 405–437.
- ¹⁰ C. F. Barenghi, V. S. L'vov, and P.-E. Roche, Experimental, numerical, and analytical velocity spectra in turbulent quantum fluid, *Proc Natl Acad Sci USA* **111**, 4683 (2014).
- ¹¹ E. Rusaouen, B. Chabaud, J. Salort, P.-E. Roche. Intermittency of quantum turbulence with superfluid fractions from 0% to 96%, *Phys. Fluids* **29**, 105108 (2017).
- ¹² L. Skrbek and K.R. Sreenivasan, Developed quantum turbulence and its decay, *Phys. Fluids* **24**, 011301 (2012).
- ¹³ J. Gao, E. Varga, W. Guo, and W. F. Vinen, Energy spectrum of thermal counterflow turbulence in superfluid helium-4, *Phys. Rev. B* **96**, 094511 (2017)
- ¹⁴ A. Marakov, J. Gao, W. Guo, S. W. Van Sciver, G. G. Ihas, D. N. McKinsey, and W. F. Vinen, Visualization of the normal-fluid turbulence in counterflowing superfluid ⁴He, *Phys. Rev. B* **91**, 094503 (2015).
- ¹⁵ M. La Mantia, P. Švančara, D. Duda, and L. Skrbek, Small-scale universality of particle dynamics in quantum turbulence, *Phys. Rev. B* **94**, 184512 (2016).
- ¹⁶ M. La Mantia, Particle dynamics in wall-bounded thermal counterflow of superfluid helium, *Phys. Fluids* **29**, 065102 (2017).
- ¹⁷ V. S. L'vov and A. Pomyalov, Theory of counterflow velocity dependence of superfluid ⁴He turbulence statistics, *Phys. Rev. B* **97**, 214513 (2018).
- ¹⁸ L. Biferale, D. Khomenko, V. L'vov, A. Pomyalov, I. Procaccia, and G. Sahoo, Turbulent statistics and intermittency enhancement in coflowing superfluid ⁴He, *Phys. Rev. Fluids* **3**, 024605 (2018).
- ¹⁹ E. Varga, J. Gao, W. Guo, and L. Skrbek, Intermittency

- enhancement in quantum turbulence in superfluid ^4He , *Phys. Rev. Fluids* **3**, 094601 (2018).
- ²⁰ L. Boue, V. S. L'vov, Y. Nagar, S. V. Nazarenko, A. Pomyalov, and I. Procaccia, Energy and vorticity spectra in turbulent superfluid ^4He from $T = 0$ to T_λ , *Phys. Rev. B* **91**, 144501 (2015).
- ²¹ D. Khomenko, V. S. L'vov, A. Pomyalov, and I. Procaccia, Counterflow induced decoupling in superfluid Turbulence. *Phys. Rev. B* **93**, 014516 (2016).
- ²² V. S. L'vov, S. V. Nazarenko and G. E. Volovik, Energy spectra of developed superfluid turbulence, *JETP Lett.* **80**, 535 (2004).
- ²³ V. S. L'vov, S. V. Nazarenko, and O. Rudenko, Bottleneck crossover between classical and quantum superfluid turbulence, *Phys. Rev. B* **76**, 024520 (2007).
- ²⁴ J. Gao, A. Marakov, W. Guo, B. T. Pawlowski, S.W. Van Sciver, G. G. Ihas, D. N. McKinsey, and W. F. Vinen, Producing and imaging a thin line of He_2^* tracer molecules in helium-4, *Rev. Sci. Instrum.* **86**, 093904 (2015).
- ²⁵ S. Pulkkinen, M. M. Mäkelä and N. Karmitsa, A generative model and a generalized trust region newton method for noise reduction, *Comput. Optim. Appl.* **57**, 129 (2014).
- ²⁶ M. Piccardi, Background subtraction techniques: a review, 2004 IEEE International Conference on Systems, Man and Cybernetics (IEEE Cat. No 04CH37583), The Hague, 3099 (2004).
- ²⁷ K. P. Iyer, K. R. Sreenivasan, P.K. Yeung, Reynolds number scaling of velocity increments in isotropic turbulence, *Physical Review E* **95**, 021101 (2017).